Journal of Fluids and Structures (2002) **16**(3), 271–294
doi:10.1006/jfls.2001.0426, available online at http://www.idealibrary.com on IDEAL®

ACTIVE WING FLUTTER SUPPRESSION USING A TRAILING EDGE FLAP

D. BORGLUND AND J. KUTTENKEULER
Department of Aeronautics, Kungliga Tekniska Högskolan
SE-100 44 Stockholm, Sweden

(Received 10 May 2000, and in final form 22 August 2001)

The aeroservoelastic behaviour of a thin rectangular wing with a controllable trailing edge flap is investigated. A rather high aspect ratio motivates a numerical model based on linear beam theory for the structural dynamics and strip theory for the unsteady aerodynamic loads. Experimental flutter testing shows good agreement with the numerical stability analysis, and the impact of the trailing edge flap on the dynamics is verified by open-loop testing. The problem of stabilizing the wing utilizing the trailing edge flap is posed, and the design of a fixed-structure feedback controller is performed using numerical optimization. The problem of maximizing closed-loop modal damping with constraints on actuator performance is solved for a sequence of flow speeds and the obtained controller is synthesized using gain scheduling. The fairly large predicted increase in critical speed is experimentally verified with satisfactory accuracy.

1. INTRODUCTION

ACTIVE FLUTTER SUPPRESSION is true multidisciplinary analysis and design, involving the interaction between elastic structures, unsteady fluid-dynamic forces and control systems. In aircraft structures, the problem of active wing flutter suppression has received much attention. Typically, an unsteady potential flow model is combined with a linear structural analysis to obtain a tool useful for control law design. The main difficulty from a control point of view lies in the representation of the unsteady aerodynamic loads. The classical approach to flutter analysis (Bisplinghoff *et al.* 1996) is based on frequency-domain aerodynamic loads, computed for simple harmonic motion. This representation can only be assumed accurate close to the flutter boundary, and in general aerodynamic loads for arbitrary motion are required to accurately predict the aeroelastic response and control system performance. The frequency-domain aerodynamic loads are most commonly generalized using rational function approximations of the exact representation.

To exemplify the significant effort devoted to theoretical studies, Edwards *et al.* (1978) and Karpel (1982) focus on the development and use of rational function approximations for the purpose of aeroelastic control. Improved gust response and increased flutter stability are demonstrated for typical section type of systems. Luton & Mook (1993) combine a general unsteady vortex-lattice method with a nonlinear structural model of a cantilever wing, to perform time-domain simulations of the resulting nonlinear aeroelastic system. While this approach eliminates the need for frequency-domain aerodynamics, it prevents the use of the vast flora of linear control techniques. By trial-and-error tuning of a simple controller, the flutter speed is significantly increased in the simulations.

In contrast, experimental demonstrations of successful closed-loop flutter suppression are rare. Experimental results on typical section type of systems are presented by Heeg (1993)

0889–9746/02/030271 + 24 $35.00/0

and Vipperman *et al.* (1998). Utilizing piezoelectric actuation, Heeg demonstrated a 20% increase of the flutter speed in wind tunnel testing. In this case, a simple single-input single-output feedback controller was used, and the analysis and design was based on rational function approximations for the aerodynamics. Vipperman *et al.* use experimental system identification in the subcritical regime and robust control law design to extend the flutter boundary by roughly 10% in the experiment.

The more difficult system of a cantilever wing has been investigated experimentally by, for example, Ghiringhelli *et al.* (1990). The capability of a straightforward eigenvalue assignment technique for control law design, based on a p–k approximation of the flutter equations, was demonstrated by significantly increasing the damping of a wing model with an actuated aileron. Substantial increase of the flutter speed was also indicated but could not be verified due to a speed limitation in the wind tunnel test. While producing simple and reliable control laws, the determination of the best location of the flutter eigenvalues is concluded to be nontrivial.

Among the more extensive efforts is the active flexible wing program at the NASA Langley Research Center. This program considered an actively controlled, statically and aeroelastically scaled, full-span wind tunnel model. Once again, linear finite element analysis was combined with a rational function approximation for the aerodynamics. Ultimately, flutter suppression while performing rapid rolling manoeuvers was demonstrated. Although an objective of the program was to use multivariable control methods, it was also concluded that classical methods were sufficient. The classical approach was completed well in advance of the optimization-based efforts and succeeded in meeting the program objectives. A summary of the classical design and further references can be found in Waszak & Srinathkumar (1995).

The more recent Benchmark Active Control Technology program at NASA is another extensive effort which deals with a multivariable typical section type of wind tunnel model in the subsonic and transonic regimes. This program has provided the aeroelastic research community with many tractable experimental results on unsteady aerodynamics and performance of various control methods. Since the first submittal of this paper, 18 related papers have been published in special sections of the *Journal of Guidance, Control and Dynamics* (Mukhopadhyay 2000*a*, *b*, 2001), of which a survey is highly recommended.

This study focusses on the flutter stability of a cantilever flexible wing in low-speed air-flow. Of particular interest is the possibility of suppressing an unexpected second bending and first torsion type of instability, as opposed to the classical mode often encountered in other studies. Unexpected instability phenomena like this should be identified, investigated and guarded against. If encountered, however, active control is one option for recovery of the initially predicted performance. The simplicity of the structural design and control system components allows for an almost complete presentation of the aeroservoelastic design process, including the modelling of frequency-domain aerodynamic forces, identification of actuator dynamics and compensation for delays in the digital control system.

An approach similar to the eigenvalue assignment technique by Ghiringhelli *et al.* (1990) is adopted for the control law design. With this approach, good performance may be obtained using simple control laws, which simplifies implementation and reduces risk. Constrained nonlinear optimization is used to design a fixed-structure controller by shifting the closed-loop p–k eigenvalues obtained from a linear aeroservoelastic stability analysis. Since only performance in terms of stability is considered, a frequency-domain representation of the aerodynamic loads is considered sufficient. Being quite similar to techniques applied in aeroelastic tailoring (Kuttenkeuler & Ringertz 1998*a*), it is also concluded that great care must be taken when using optimization for design.

Experimental verification of the accuracy of the aeroservoelastic analysis and control law design is emphasized. Of particular experimental interest was the possibility of using a non-contact optical measurement system to monitor the elastic deformation of the wing. The present system has been proven very useful in various aeroelastic wind-tunnel experiments [see, for example, Kuttenkeuler (2000)], but is for the first time at KTH used for real-time closed-loop control. The results presented in this paper are also part of the first author's Ph.D. thesis (Borglund 2000).

2. AEROSERVOELASTIC MODELLING

The aeroservoelastic system to be investigated in the present paper is illustrated in Figure 1. A cantilevered thin elastic wing with a rectangular planform is subjected to unsteady aerodynamic loads due to low-speed air-flow. At some sufficiently high flow speed, the wing will suffer a divergence or flutter-type aeroelastic instability.

As shown in the figure, the wing is equipped with a controllable trailing edge flap, or aileron. The idea to be exploited is that by proper control of the aileron, the operating range of the wing (in terms of aeroelastic stability) may be extended without weight penalty.

2.1. Equations of Motion

The planform of the wing–aileron assembly is given by the wing semispan l and semichord b, and the aileron length l_a and semichord b_a. The wing structure consists of a thin elastic plate with constant thickness h. The wing is assumed to have such a high aspect ratio that the small-amplitude motion is modelled with sufficient accuracy using a linear Euler-type beam model. Using this approximation, the wing is divided into the inner partition $0 \leq y < l - l_a$ and the outer partition $l - l_a \leq y \leq l$, between which the location of the elastic axis differs by a distance $e = b_a$ due to the aileron cut-out (see Figure 1). The beam approximation is based on the assumption that the wing is chordwise rigid, and the deformation of the wing is thus described by the deflection $w(y, t)$ and twist angle $\theta(y, t)$ of the elastic axis, where t denotes time.

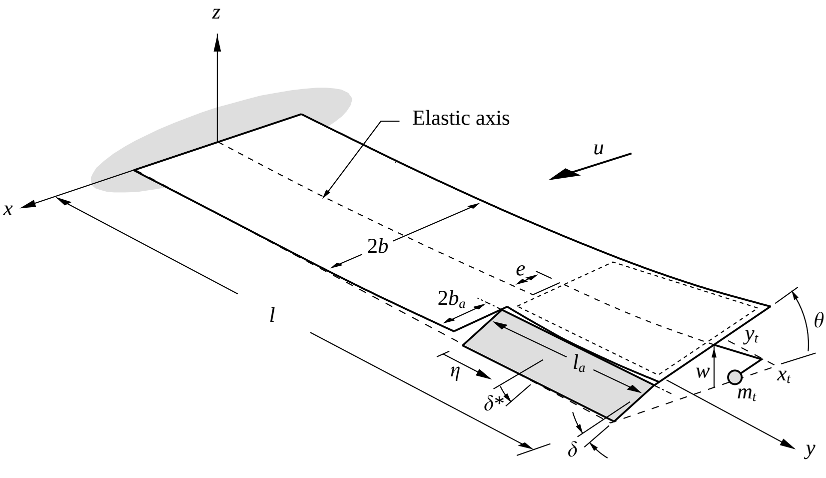

Figure 1. A cantilever wing in low-speed air-flow.

The aileron has the same thickness as the wing but is considered rigid, with mass m_a. It is attached to the wing with an inner hinge at $y = l - l_a$ and an outer hinge at $y = l$. Assuming ideal hinges and that the hinge axis is free to slide at the inner hinge, the aileron assembly will not contribute to the structural stiffness for small elastic deformations of the wing. Hence, only the transfer of inertial and aerodynamic loads from the aileron to the wing is considered. The aileron hinge moment is assumed to be transferred to the wing at the wing tip ($y = l$), where an actuator specifies the aileron deflection $\delta(t)$. The actuator assembly clamped to the wing tip is modelled rigid (assumed to have no aerodynamic influence) with mass m_t and principal mass moments of inertia J_x, J_y and J_{xy}, respectively, with the centre of mass located at coordinates x_t and y_t relative to the elastic axis at the wing tip (see Figure 1).

Assuming Kelvin–Voigt-type structural damping, the linear equations of motion for each wing partition may be written in the form

$$m_w \ddot{w} - m_w s \ddot{\theta} + D_w^* \dot{w}'''' + D_w w'''' = L_w, \tag{1}$$

$$J_\theta \ddot{\theta} - m_w s \ddot{w} - D_\theta^* \dot{\theta}'' - D_\theta \theta'' = M_\theta, \tag{2}$$

where a prime denotes differentiation with respect to y and a dot with respect to t. The wing mass and mass-moment of inertia per spanwise unit length are denoted m_w and J_θ, respectively. Although included in the equations of motion for completeness, there is no inertial bending–torsion coupling in the present case since the difference between the chordwise locations of the inertial axis and the elastic axis is $s = 0$. The wing bending and torsional stiffnesses are represented by D_w and D_θ, while D_w^* and D_θ^* are coefficients determining the structural damping. Finally, $L_w(y, t)$ and $M_\theta(y, t)$ are the applied force and pitching moment per unit length.

The applied loads are composed of unsteady aerodynamic loads on the wing itself (both partitions) and inertial as well as aerodynamic loads from the aileron (transferred through the hinges to the outer partition). Given the applied loads, the equations of motion for the inner and outer wing partitions are coupled through the kinematic constraints

$$w_1(t) = w_2(t) - \mathrm{e}\theta_2(t), \tag{3}$$

$$w_1'(t) = w_2'(t), \qquad \theta_1(t) = \theta_2(t), \tag{4, 5}$$

at $y = l - l_a$, where the subscript "1" refers to the inner partition and "2" to the outer.

The boundary conditions for the cantilever wing at $y = 0$ are simply

$$w = w' = \theta = 0, \tag{6}$$

while the boundary conditions defining the transverse force and moments at the wing tip are

$$D_w^* \dot{w}''' + D_w w''' + m_t \ddot{w} + m_t y_t \ddot{w}' - m_t x_t \ddot{\theta} = 0, \tag{7}$$

$$D_w^* \dot{w}'' + D_w w'' + m_t y_t \ddot{w} + (J_x + m_t y_t^2)\,\ddot{w}' - (J_{xy} + m_t x_t y_t)\,\ddot{\theta} = 0, \tag{8}$$

$$-\,D_\theta^* \dot{\theta}' - D_\theta \theta' - m_t x_t \ddot{w} - (J_{xy} + m_t x_t y_t)\ddot{w}' + (J_y + m_t x_t^2)\,\ddot{\theta} = 0, \tag{9}$$

which correspond to the inertia forces from the actuator assembly.

2.2. WING-AILERON COUPLING

While the described aileron assembly has advantages from a mechanical and structural modelling point of view, aerodynamic concerns are introduced. Even if air-flow through a small gap between the wing trailing edge and the aileron leading edge is prevented, bending of the wing may result in a chordwise step at the wing–aileron intersection (indicated in Figure 1). Another, perhaps more important, elastic coupling is that torsional deformation introduces a local aileron deflection. In addition to the motion specified by the actuator at $y = l$, the aileron will rotate with the wing tip (independently of the local twist angle). Accounting for this and considering that the local aileron deflection is defined relative to the local twist angle $\theta(y, t)$, the local aileron deflection $\delta^*(y, t)$ (see Figure 1) is given by

$$\delta^*(y, t) = \{\delta(t) + \theta_2(t)\} - \theta(y, t), \tag{10}$$

where $\theta_2(t) = \theta(l, t)$ is the twist angle at the wing tip.

A first-order approximation of the elastic coupling is obtained by considering the free vibrations of the cantilever wing when $l_a \ll l$. The elastic deformation of the outer wing partition can then be assumed linear,

$$w(y, t) = w_1(t) + \eta\{w_2(t) - w_1(t)\}, \tag{11}$$

$$\theta(y, t) = \theta_1(t) + \eta\{\theta_2(t) - \theta_1(t)\}, \tag{12}$$

where $\eta = \{y - (l - l_a)\}/l_a \in [0, 1]$ is the scaled local length coordinate shown in Figure (1) and $w_1(t) = w(l - l_a, t)$, $w_2(t) = w(l, t)$, etc. The approximate deformation described by equations (11) and (12) is indicated by the dashed boundary in Figure 1. Clearly, such a deformation will not result in any chordwise step. Hence, a reasonable approximation is to neglect the influence due to a possible chordwise step and use

$$\delta^*(y, t) = \delta(t) + (1 - \eta)\{\theta_2(t) - \theta_1(t)\} \tag{13}$$

for the true local aileron deflection, obtained by inserting equation (12) into (10).

2.3 AERODYNAMIC MODEL

Justified by the high aspect ratio, Theodorsen's two-dimensional theory in the frequency domain (Theodorsen 1935) is used for the unsteady aerodynamic loads. Theodorsen derives the lift $L(t)$ and pitching moment $M(t)$ on a two-dimensional thin airfoil, oscillating with frequency ω in an air-flow with freestream velocity u and density ρ. In terms of the set of variables $q(y, t) = \{w \ \theta \ \delta^*\}$, the result can be written in the form

$$L(y, t) = \sum_{i=1}^{3} \rho(L_{\ddot{q}_i}\ddot{q}_i + uL_{\dot{q}_i}\dot{q}_i + u^2 L_{q_i}q_i) \tag{14}$$

and a corresponding expression for the moment $M(y, t)$. The lift coefficients $\{L_{\ddot{q}_i} \ L_{\dot{q}_i} \ L_{q_i}\}$ depend on the semichord b, the reduced frequency of oscillation $k = \omega b/u$, the distance from the midchord to the elastic axis (b_a) and the distance from the midchord to the aileron hinge axis ($b - 2b_a$). The same holds for the moment coefficients $\{M_{\ddot{q}_i} \ M_{\dot{q}_i} \ M_{q_i}\}$.

A direct use of Theodorsen's lift and moment in the equations of motion represents a model where the aerodynamic load on the aileron is transferred to the wing along the wing–aileron intersection. This is a convenient approximation for the actual load transfer, but a slight rearrangement of Theodorsen's result provides a two-dimensional formulation which can be used for modelling of the true load transfer. In Appendix A, the contribution $L^a(y, t)$ to the lift from the aileron partition of the two-dimensional airfoil is derived, resulting in

$$L^a (y, t) = \sum_{i=1}^{3} \rho(L^a_{\ddot{q}_i} \ddot{q}_i + uL^a_{\dot{q}_i} + u^2 L^a_{q_i} q_i). \tag{15}$$

Given the total lift (14), the lift on the wing partition is simply $L^w(y, t) = L(y, t) - L^a(y, t)$. As shown in Appendix A, the moment can be separated in a similar fashion utilizing the aileron hinge moment $M^\delta(y, t)$. With this formulation the aileron lift and hinge moment distributions can be integrated over the aileron for the total lift and moments

$$L_a(t) = \int_{l-l_a}^{l} L^a(y, t)\,\mathrm{d}y, \tag{16}$$

$$M_a(t) = \int_{l-l_a}^{l} yL^a(y, t)\,\mathrm{d}y, \tag{17}$$

$$M_\delta(t) = \int_{l-l_a}^{l} M^\delta(y, t)\,\mathrm{d}y, \tag{18}$$

which are then transferred to the wing through the hinges. In the present work, the computation of the total loads (16)–(18) is simplified using the approximations (11)–(13) in the aileron load distributions. Straightforward integration yields expressions in the kinematic variables $\{w_1\,\theta_1\,w_2\,\theta_2\,\delta\}$, in a form similar to equation (15).

Next, the loads from the aileron are transferred to the elastic axis at $y = l - l_a$ and l. Recalling that the aileron hinge moment is transferred at $y = l$, a force and moment equilibrium for the aileron gives

$$L_1(t) = L_a(t) - L_2(t), \qquad M_1(t) = -(b - b_a)L_1(t), \tag{19, 20}$$

$$L_2(t) = M_a(t)/l_a, \qquad M_2(t) = M_\delta(t) - (b - b_a)L_2(t), \tag{21, 22}$$

where $L_1(t)$ is the lift from the aileron at $y = l - l_a$ etc.

The inertia forces from the aileron may be derived using for example the rigid-body equations of motion. Note, however, that exactly the same approach as for the aerodynamic loads can be used by utilizing the aileron mass distribution. The equations of motion for the outer partition are now formulated by inserting the distributed loads $L^w(y, t)$ and $M^w(y, t)$ as well as the loads from the aileron (in the generalized sense) into equations (1) and (2). The equations of motion for the inner partition are given by direct application of Theodorsen's lift and moment for the case without an aileron.

2.4. DISCRETIZED EQUATIONS OF MOTION

The continuous equations of motion are discretized using beam finite elements with the nodal degrees of freedom $\{w\ w'\ \theta\}$ (Cook *et al.* 1989). Denoting the global vector of nodal displacements $\mathbf{w}$, the discretized equations of motion can be expressed in the form

$$\begin{aligned} &\mathbf{M}\ddot{\mathbf{w}} + \mathbf{D}\dot{\mathbf{w}} + \mathbf{K}\mathbf{w} - \rho(\mathbf{Q}_2\ddot{\mathbf{w}} + u\mathbf{Q}_1(k)\dot{\mathbf{w}} + u^2\mathbf{Q}_0(k)\mathbf{w}) \\ &= \mathbf{q}_a\ddot{\delta} + \rho(\mathbf{q}_2\ddot{\delta} + u\mathbf{q}_1(k)\ddot{\delta} + u^2\mathbf{q}_0(k)\delta), \end{aligned} \tag{23}$$

where

$$\mathbf{K} = \mathbf{K}_w + \mathbf{K}_\theta, \qquad \mathbf{D} = \alpha_w \mathbf{K}_w + \alpha_\theta \mathbf{K}_\theta \tag{24, 25}$$

and the parameters $\alpha_w = D_w^*/D_w$ and $\alpha_\theta = D_\theta^*/D_\theta$ have been introduced for convenience. The mass matrix **M**, the bending and torsional stiffness matrices $\mathbf{K}_w$ and $\mathbf{K}_\theta$ as well as the aerodynamic mass matrix $\mathbf{Q}_2$ are all real and symmetric positive definite, while the aerodynamic damping and stiffness matrices $\mathbf{Q}_1(k)$ and $\mathbf{Q}_0(k)$ are, in general, complex and nonsymmetric. Explicit aileron motion $\delta(t)$ induces aerodynamic loads represented by the vectors $\mathbf{q}_2$, $\mathbf{q}_1(k)$ and $\mathbf{q}_0(k)$, and mass coupling determined by $\mathbf{q}_a$.

2.5. ACTIVE CONTROL

Writing equation (23) in state-equation form with $\delta(t)$ as control variable is nontrivial due to the dependency on $\dot{\delta}(t)$ and $\ddot{\delta}(t)$. However, this obstacle is resolved by introducing an actuator model having $\delta(t)$ and $\dot{\delta}(t)$ as dynamic states. The most simple model that fulfils this criterion and captures the essential dynamics of a servo actuator is given by

$$\ddot{\delta} + 2\omega_0\zeta\dot{\delta} + \omega_0^2\delta = \omega_0^2\delta_s, \tag{26}$$

where ω_0 and ζ determine the speed and damping of the servo response, respectively, and $\delta_s(t)$ is the setpoint for the servo. Introducing the state vector $\mathbf{w}_s(t) = [\delta, \dot{\delta}]^{\mathrm{T}}$ gives the standard state-equation form

$$\dot{\mathbf{w}}_s = \begin{bmatrix} 0 & 1 \\ -\omega_0^2 & -2\omega_0\zeta \end{bmatrix} \mathbf{w}_s + \begin{Bmatrix} 0 \\ \omega_0^2 \end{Bmatrix} \delta_s. \tag{27}$$

Now, the crucial observation is that the right-hand side of equation (23) can be written in terms of the state vector $\mathbf{w}_s(t)$ and its first time derivative. Consequently, by forming the augmented state vector $\mathbf{w}_p(t) = [\mathbf{w}, \dot{\mathbf{w}}, \mathbf{w}_s]^{\mathrm{T}}$ the equations of motion (23) and the servo dynamics (27) can be merged into the generalized state equation

$$\mathbf{M}_p\dot{\mathbf{w}}_p = \mathbf{Q}_p(k, u)\mathbf{w}_p + \mathbf{q}_p\delta_s, \qquad \mathbf{y} = \mathbf{C}_p\mathbf{w}_p, \tag{28, 29}$$

having the setpoint $\delta_s(t)$ for the servo as input and, in addition, some measured entities $\mathbf{y}(t)$ in the form (29) as output.

The control objective in this study is to improve the stability of the wing by feedback control of the aileron. Consider the block diagram in Figure 2 where $P(u)$ represents the aeroservoelastic plant and the remaining blocks represent a digital controller. Based on the measured outputs $\mathbf{y}(t)$ and the flow speed u, the task of the controller is to compute a setpoint $\delta_s(t)$ such that the aeroservoelastic response $\mathbf{w}_p(t)$ due to a flow disturbance $\mathbf{d}(t)$ (not accounted for in the model) is efficiently suppressed.

The sampling and computational delays introduced when using a digital controller are represented by the blocks K_T and K_Δ, respectively. A modified continuous design as described in Stevens & Lewis 1992 is used, where continuous approximations of the discrete dynamics are used in the design of the controller $K(u)$. A 2-pole-2-zero Padé approximation of the transfer function for a sample-and-hold process with period T seconds can be written in the state equation form

$$\dot{\mathbf{w}}_T = \begin{bmatrix} 0 & 1 \\ -20/T^2 & -8/\mathrm{T} \end{bmatrix} \mathbf{w}_T + \begin{Bmatrix} 0 \\ 1 \end{Bmatrix} \boldsymbol{\delta}_T, \tag{30}$$

$$\delta_s = [40/3T^2 \quad -14/3T]\,\mathbf{w}_T + \delta_T/3, \tag{31}$$

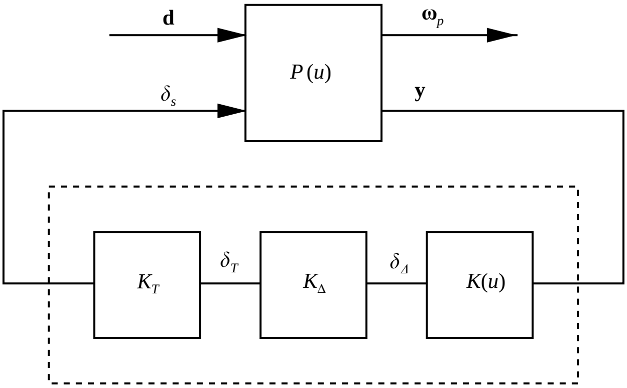

Figure 2. Block diagram illustrating the control objective.

where the state vector $\mathbf{w}_T(t)$ comprises two states. As shown in the figure, the input $\delta_T(t)$ is the signal to be sampled and the output $\delta_S(t)$ is the setpoint for the servo. The same approximation for a computational delay of Δ seconds yields

$$\dot{\mathbf{w}}_\Delta = \begin{bmatrix} 0 & 1 \\ -12/\Delta^2 & -6/\Delta \end{bmatrix} \mathbf{w}_\Delta + \begin{Bmatrix} 0 \\ 1 \end{Bmatrix} \boldsymbol{\delta}_\Delta, \tag{32}$$

$$\delta_T = [0 \quad -12/\Delta]\, \mathbf{w}_\Delta + \delta_\Delta, \tag{33}$$

where $\delta_\Delta(t)$ is the input signal to be delayed (see the figure) and $\mathbf{w}_\Delta(t)$ is a state vector with two states.

The modified aeroservoelastic plant accounting for servo dynamics as well as sampling and computational delays is now obtained by merging equations (28)–(33). The corresponding state equation can be written in terms of the state vector $\mathbf{w}_m(t) = [\mathbf{w}_p, \mathbf{w}_T, \mathbf{w}_\Delta]^{\mathrm{T}}$,

$$\mathbf{M}_m \dot{\mathbf{w}}_m = \mathbf{Q}_m(k, u)\mathbf{w}_m + \mathbf{q}_m \delta_\Delta, \qquad \mathbf{y} = \mathbf{C}_m \mathbf{w}_m, \tag{34, 35}$$

having the output $\delta_\Delta(t)$ from the controller $K(u)$ as input variable.

In this study, a simple output feedback controller is used, defined by

$$\delta_\Delta = \mathbf{k}^{\mathrm{T}}(u)\,\mathbf{y} = \mathbf{k}^{\mathrm{T}}(u)\,\mathbf{C}_m \mathbf{w}_m, \tag{36}$$

where $\mathbf{k}(u)$ is a vector of feedback gains which may depend on the flow speed u. Inserting the control law (36) into the state equation (34) and transforming to the frequency domain using $\mathbf{w}_m(t) = \hat{\mathbf{w}}_m \mathrm{e}^{pt}$ yields the nonlinear generalized eigenvalue problem

$$\left[\hat{p}\mathbf{M}_m - \frac{b}{u}(\mathbf{Q}_m(k, u) + \mathbf{q}_m \mathbf{k}^{\mathrm{T}}(u)\mathbf{C}_m)\right] \hat{\mathbf{w}}_m = \mathbf{0}, \tag{37}$$

where the reduced eigenvalue $\hat{p} = pb/u$ has been introduced for convenience. The nonlinearity is due to the dependence on the reduced frequency $k = \omega b/u$, which is the imaginary part of $\hat{p}$. For a given flow speed u and feedback gain vector $\mathbf{k}(u)$ the eigenvalue problem (37) is solved iteratively using the so-called p–k method (Bäck & Ringertz 1997). The predicted critical flow speed u_{pred} at which an aeroservoelastic instability develops is computed by solving the eigenvalue problem for a sequence of increasing flow speeds, until an eigenvalue with positive real part is detected.

3. EXPERIMENTAL APPROACH

A schematic layout of the wind tunnel experiment is shown in Figure 3. All testing was performed in a low-speed wind tunnel at KTH. The cross section of the 3·6 m^2 test-section is square with corner fillets. The environmental test conditions were room temperature and atmospheric pressure throughout the tests, with air density close to $\rho = 1{\cdot}18$ kg/m^3. This value is therefore used in all subsequent analyses.

The very flexible wing was mounted vertically in the wind tunnel, hanging from the ceiling of the test-section. Using the notation introduced in Figure 1, the wing has semispan $l = 1\,200$ mm and semichord $b = 120$ mm (giving an aspect ratio of 10). The wing was made of orthotropic glassfibre-epoxy laminate with nominal thickness 3 mm, with the main stiffness axis aligned with the wing x- and y-coordinate axis. Thus, there is no bending/torsion coupling due to the material anisotropy. The aileron with the same thickness, length $l_a = 352$ mm and semichord $b_a = 30$ mm, consisted of a carbon fibre sandwich plate for high stiffness and low weight. To reduce air-flow through the small gap between the wing and aileron, a thin plastic film was used to cover the gap (attached only to the wing).

Two full-chord, slightly swept, vertical winglets were mounted at the wing tip to reduce the finite span effects not taken into account in the two-dimensional aerodynamic model. Two inner winglets were also mounted, mostly to provide a fixture for the inner aileron hinge. The inner winglets have $\frac{5}{12}$ the dimensions of the outer, which are given in Figure 3.

The aileron is controlled by a high-performance linear electric servo, enclosed by a NACA 0012 airfoil-shaped cover at the wing tip. A linear potentiometer for measurement of the aileron deflection is also part of the wing tip assembly. Not to interact with the thin wing aerodynamics, 35 μm thick adhesive copper foil was used for the wires to the servo and potentiometer. The aerodynamic impact of the $\Delta l = 43$ mm rigid extension of the wing is neglected.

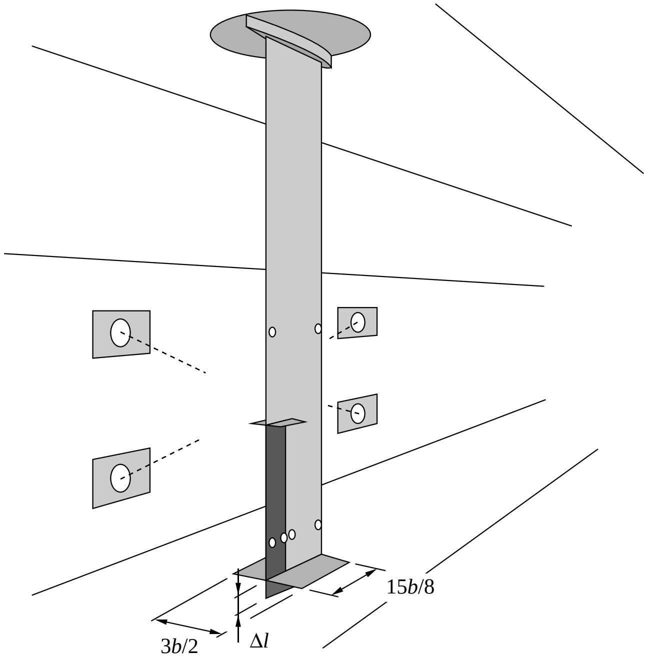

Figure 3. Schematic layout of the wind tunnel experiment.

TABLE 1
Coordinates of the reflecting markers

Marker	x (mm)	y (mm)
1	– 112·5	636
2	112·5	636
3	– 112·5	1 112
4	44·0	1 112
5	74·5	1 112
6	112·5	1 112

The aeroelastic deformation of the wing was monitored by a noncontact optical measurement system, capable of real-time three-dimensional tracking of reflecting markers attached to the wing. As shown in Figure 3, the present system is based on four CCD cameras with built-in infrared flashes, mounted in the wind tunnel walls. Hemi-spherical markers with 5 mm radius were used to measure the out-of-plane displacements at specific locations on the wing. Although flat markers can be used, the hemispherical markers provided higher robustness and accuracy. For the present configuration, the marker displacements were measured with a resolution of only a few hundreds of a millimeter. For more details on the optical system the reader is referred to Kuttenkeuler (2000).

A numerical model with eight finite elements for the inner wing partition and four for the outer is used throughout the study. Based on this, six markers were attached to the wing at two different spanwise locations, both coalescing with nodes in the finite element model. The marker configuration is shown in Figure 3, drawn on the nearest side of the wing for the sake of clarity. The coordinates of the marker locations are given in Table 1, where the markers are numbered in consecutive order from the midwing leading edge marker to the aileron trailing edge marker. The locations of the four markers on the wing were chosen to give a reasonable observability of the dominant aeroelastic modeshapes. Expressed in terms of the deflection and twist angle of the elastic axis, the wing deflections at the marker locations are easily written in the form (29). By placing two markers on the aileron as well, the optical measurement provided a simultaneous acquisition of the aileron deflection at $\eta = \frac{3}{4}$. This feature will be utilized in Section 4.2.

3.1. STRUCTURAL PROPERTIES

Since the wing is mounted vertically, it may be necessary to consider gravitational effects. Neglecting the gravity forces from the aileron, this can be accounted for in the bending dynamics by introducing the term

$$f_g(y,t) = g\left\{m_w w' - \left(\int_y^l m_w\,dy + m_t\right)w''\right\} \tag{38}$$

into the left-hand side of the equation of motion (1) for the outer wing partition (g is the gravity acceleration), and adding the transverse force $T_g = g m_t w'$ and bending moment $M_g = g m_t y_t w'$ to the left-hand side of the boundary conditions (7) and (8), respectively (Païdoussis 1998). The corresponding term for the inner wing partition is obtained by simply replacing m_t with the total mass of the outer partition, and taking the integral to $y = l - l_a$. The result in the discretized equations of motion is a contribution $\mathbf{K}_g$ to the stiffness matrix (24). The described correction is included in the aeroservoelastic model, mostly to isolate the structural stiffness in the verification of the structural model. The gravity forces from the aileron are approximated by simply adding m_a to the total wing tip mass m_t.

The wing tip and inner winglet assemblies are modelled as rigid bodies clamped to the wing. The mass properties of each assembly were obtained by assembling the corresponding properties of its components. For each component, the mass, dimensions and location of the centre of mass were measured experimentally, while the rotary inertias were estimated analytically. The resulting mass properties and coordinates of the mass centres are given in Table 2. The corresponding properties of the aileron are also given.

Given the wing laminate density ρ_w and chord c_w, the rectangular wing section has mass per unit length $m_w = \rho_w c_w h$ and mass moment of inertia per unit length $J_\theta = m_w(c_w^2 + h^2)/12$. Note that $c_w = 2b$ in the inner partition and $c_w = 2(b - b_a)$ in the outer. Based on plate theory, the beam stiffnesses are $D_w = c_w D_{22}$ and $D_\theta = 4c_w D_{66}$, where D_{22} and D_{66} are the orthotropic plate stiffnesses defined in Weisshaar & Foist (1985). In the same manner, $D_w^* = c_w D_{22}^*$ and $D_\theta^* = 4c_w D_{66}^*$, where D_{22}^* and D_{66}^* are the corresponding coefficients in the viscoelastic plate model. The plate stiffnesses of the wing laminate was determined from a rectangular test specimen using the dynamic method described by Kuttenkeuler (1999). The experimentally determined laminate properties can be found in Table 3. For completeness, all the orthotropic plate stiffnesses are presented.

3.2. Structural Dynamics

The frequency and modal damping of the free vibrations of the hanging cantilever wing (with the aileron fixed at $\delta = 0$) is computed by solving the eigenvalue problem (37) for

Table 2
Experimentally determined mass properties

Property	Inner winglet	Wing tip	Aileron	Unit
m	$4{\cdot}11 \times 10^{-2}$	$4{\cdot}60 \times 10^{-1}$	$6{\cdot}57 \times 10^{-2}$	kg
J_x	$1{\cdot}73 \times 10^{-5}$	$7{\cdot}15 \times 10^{-4}$	$6{\cdot}78 \times 10^{-4}$	kg m^2
J_y	$4{\cdot}74 \times 10^{-5}$	$2{\cdot}34 \times 10^{-3}$	$1{\cdot}98 \times 10^{-5}$	kg m^2
J_{xy}	0	$-2{\cdot}17 \times 10^{-5}$	0	kg m^2
x	70·5	− 2·0	90·0	mm
y	634·5	1209	1024	mm

Table 3
Experimentally determined laminate properties

Property	Value	Unit
h	3·06	mm
ρ_w	1926	kg/m^3
D_{11}	65·9	N m
D_{12}	9·54	N m
D_{22}	59·4	N m
D_{66}	14·1	N m
D_{22}^*	$9{\cdot}66 \times 10^{-3}$	N m s
D_{66}^*	$3{\cdot}37 \times 10^{-3}$	N m s

TABLE 4
Comparison between predicted and experimental eigenfrequencies

Mode	f_{pred} (Hz)	f_{exp} (Hz)
1B	1·0	1·0
2B	5·9	5·9
1T	7·3	7·4
3B	17·0	16·7
2T	21·3	22·5
4B	34·3	34·3
3T	39·0	42·9
5B	54·5	54·0
4T	62·0	72·3
6B	80·9	78·5

$u = 0$ and $\mathbf{k} = \mathbf{0}$. The vibration analysis thus obtained accounts for both gravity (to some extent) and the added mass due to the surrounding air. Neglecting the structural damping ($D^*_{22} = D^*_{66} = 0$), the 10 lowest predicted eigenfrequencies (f_{pred}) are compared to experimental values (f_{exp}) in Table 4. The experimental frequencies were obtained by modal analysis. The mode denoted 1B is dominated by the first decoupled bending mode, 2T by the second torsion mode, etc. All the bending modes show excellent agreement between theory and experiment, while the accuracy for the torsion modes deteriorates with frequency. Considering the simplicity of the structural model, the general agreement is considered to be satisfactory.

The values of the two viscoelastic parameters D^*_{22} and D^*_{66} given in Table 3 were determined by matching the modal damping (the real part of the eigenvalues) of the second bending (2B) and first torsional (1T) eigenmodes to experiments. Accounting for the damping has a negligible influence on the frequencies in Table 4.

3.3. FLUTTER EXPERIMENTS

The accuracy of the aeroelastic stability analysis was investigated by performing flutter testing of the wing, with the aileron fixed at $\delta = 0$. Figure 4 shows a root-locus plot of the four leading eigenvalues obtained by solving the eigenvalue problem (37) from $u = 5$ m/s (marked by "$\circ$") to critical speed (marked by "$\times$"). Mode A is a flutter mode influenced by the second bending and first torsional structural modes, with frequency in the 6 Hz range. Mode B is the classical flutter mode which couples the first bending and first torsional modes. The frequency of mode B decreases significantly with flow speed, ending up in the 3 Hz range. The low-frequent flutter mode C is mostly influenced by the first structural bending mode, and is stabilized for increasing flow speed. At $u = 16{\cdot}6$ m/s the divergence mode D appears, which is the mode that finally becomes unstable at $u = 20{\cdot}8$ m/s.

The wing is thus predicted to diverge at the critical speed $u_{\text{pred}} = 20{\cdot}8$ m/s. However, in the wind tunnel test the wing suffered a flutter instability at $u_{\text{exp}} = 15{\cdot}4$ m/s. By recording the limit cycle motion with the optical system, a closer investigation revealed that the experimental flutter frequency was 6·4 Hz. Further, the modeshape was clearly influenced by the second structural bending mode. With these results at hand, the somewhat unexpected result can be explained by considering the root-locus plot again. At $u = 16{\cdot}2$ m/s mode A is the closest to instability (marked by "*" in the root-locus plot), but is then

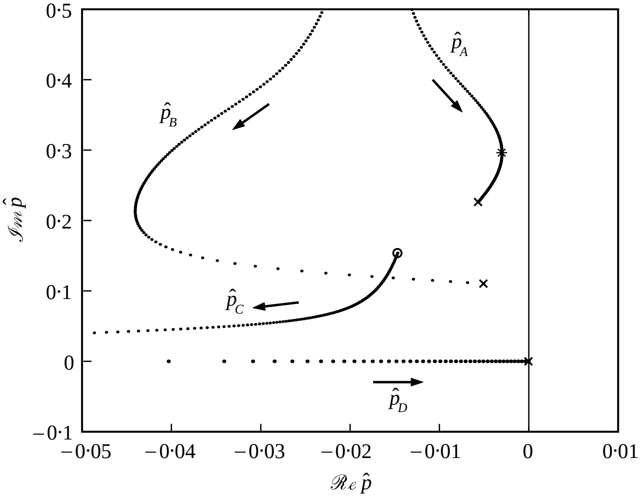

Figure 4. Open-loop root-locus plot. The arrows indicate the direction of movement of poles with increasing flow speed u. The pole locations at the predicted critical speed are marked by " × ".

stabilized again for increasing speed. The predicted frequency at this speed is 6·4 Hz. The conclusion is that mode A becomes unstable in the experiment at a speed which is supported by the stability analysis. While the aeroelastic analysis predicts the flutter frequency of this mode fairly well, it is not fully capable of predicting the modal damping. Increasing the flow speed further resulted in a rapid growth of the flutter amplitude, which made further (reasonably safe) experimental investigations impossible.

4. ACTIVE CONTROL

Provided that the aeroservoelastic analysis is sufficiently accurate for control law design, a stabilization of mode A could be very profitable in terms of increased flutter speed. For example, suppressing the mode A flutter without affecting the other modes would, in theory, give an approximately 30% increase in critical speed. An initial strategy for the control law design is thus to find a controller in the form (36) that stabilizes mode A exclusively. Prior to giving an example of such a design, some results on the actuator performance and the response due to aileron motion are presented.

4.1. SERVO IDENTIFICATION

As suggested by Waszak & Fung (1996), the parameters w_0 and ζ in the actuator model (27) are identified by matching the magnitude and phase of the servo frequency response function (FRF) to experimental data. A personal computer with the LabVIEW software (Johnson 1994) was used to command a sinusoidal aileron motion with 6° amplitude, with the setpoint updated at a rate of 100 Hz. The aileron response was measured for a sequence of frequencies in the range 2–8 Hz (the expected bandwidth of the aeroservoelastic response), using the potentiometer mounted at the wing tip. Data reduction using fast Fourier transform (FFT) analysis gave the experimental frequency response represented by the discrete data points in Figure 5.

The hold delay introduced by the digital control of the servo is compensated for by merging the servo dynamics (27) with equations (30) and (31) and using δ_T as input. This

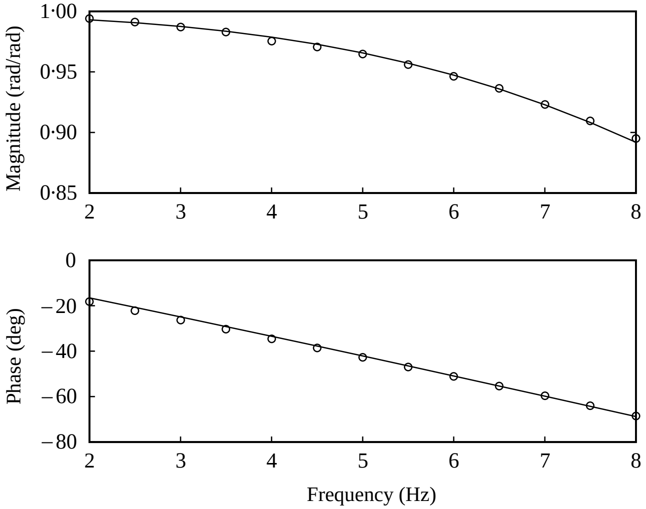

Figure 5. Servo frequency response: ○, measured; ——, predicted.

means that the FRF between δ_T and δ, with $T = 1/100$ s, is used for the identification. The servo parameters are determined by minimizing the weighted sum square error

$$\varepsilon^2(\omega_0, \zeta) = \sum_{i=1}^{n} (\Delta\mu)_i^2 + \gamma \sum_{i=1}^{n} (\Delta\varphi)_i^2 \tag{39}$$

of the $n = 13$ magnitude and phase errors $\Delta\mu = \mu_{\mathrm{exp}} - \mu_{\mathrm{pred}}$ and $\Delta\varphi = \varphi_{\mathrm{exp}} - \varphi_{\mathrm{pred}}$, respectively. The weight γ determines how the magnitude and phase are emphasized in the identification. Using $\gamma = 1/100\ \mathrm{rad}^{-1}$ resulted in $\omega_0 = 84{\cdot}3$ rad/s and $\zeta = 0{\cdot}754$. The corresponding FRF is represented by the solid lines in Figure (5). Good agreement between the predicted and experimental FRFs is achieved, indicating that the servo dynamics is well modelled by equation (27).

4.2. OPEN-LOOP EXPERIMENTS

Experimental open-loop testing was performed in order to verify the influence of the aileron on the system dynamics. Since the accuracy of the aeroservoelastic analysis close to the flutter boundary is of particular interest, the flow speed $u = 15$ m/s was chosen in the open-loop experiments. The displacement response of the wing due to sinusoidal aileron motion in the range 2–8 Hz was measured at a rate of 240 Hz using the optical system. The commanded amplitude for the aileron deflection was 3° throughout the measurements, and the setpoint for the servo was updated at a rate of 100 Hz.

The aileron deflection at the spanwise location $\eta = \frac{3}{4}$ was estimated based on the measured out-of-plane marker displacements of markers 3 and 4 on the wing and markers 5 and 6 on the aileron (see Figure 3). Accurate time control is of vital importance to obtain relevant phase data. In this respect, the main advantage of measuring the aileron deflection using the optical system is that the aileron and wing motion are measured simultaneously.

The magnitude and phase of the experimental FRF between the aileron deflection and the marker 1 displacement (midwing-leading edge) are shown in Figure 6. At low frequencies the wing displayed a motion resembling the first structural bending mode. While a very

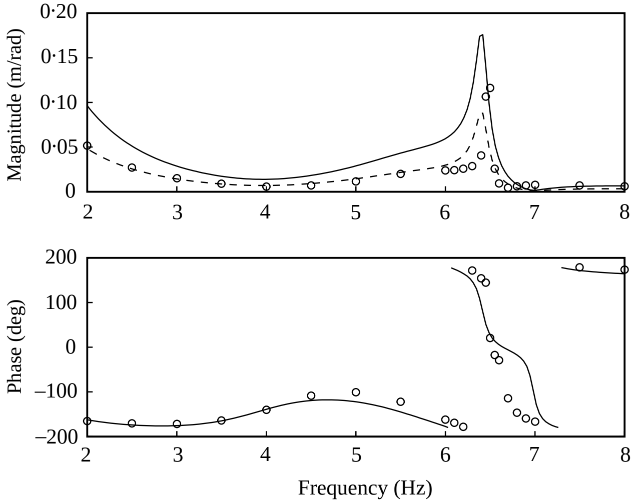

Figure 6. Experimental (◦), predicted (–) and updated predicted (––) open-loop frequency response for marker 1, at $u = 15$ m/s.

modest response was found in the 3–5 Hz range, a sharp resonance with a second bending-first torsion modeshape was observed at 6·4 Hz, revealing the approaching flutter instability.

The theoretical FRFs between the true aileron deflection $\delta^*(y, t)$ and the marker displacements may be computed as follows. Inserting a known aileron motion (at the wing tip) $\delta(t) = \hat{\delta} \mathrm{e}^{\mathrm{i}\omega t}$ and an expected response $\mathbf{w}(t) = \hat{\mathbf{w}} \mathrm{e}^{\mathrm{i}\omega t}$ (where $\hat{\mathbf{w}}$ is complex) into the equations of motion (23) results in a linear system of equations for the vector $\mathbf{z} = \hat{\mathbf{w}}/\hat{\delta}$ in the form

$$\mathbf{Q}(\omega, u)\,\mathbf{z} = \mathbf{q}(\omega, u). \tag{40}$$

This vector clearly represents the FRFs between the aileron deflection at the wing tip and the nodal displacements in the finite element model. With known FRFs z_{θ_1} and z_{θ_2} (elements of $\mathbf{z}$) for the twist angles $\theta_1(t)$ and $\theta_2(t)$, the FRFs between the true aileron deflection in (13) and the nodal displacements in the finite element model are given by

$$\mathbf{z}^* = \frac{\mathbf{z}}{\mathbf{1} + (1 - \eta)(z_{\theta_2} - z_{\theta_1})}. \tag{41}$$

Finally, the FRFs for the marker displacements follow from the corresponding output relation in the form (29).

The theoretical FRF for the marker 1 displacement is represented by the solid lines in Figure 6, where it is observed that the general characteristics are well represented by the model. Both the resonance frequency and the phase are predicted with good accuracy, while the magnitude is clearly over-predicted throughout the entire frequency range. Strip theory is well known to over-predict the unsteady aerodynamic loads (Bisplinghoff *et al.* 1996), especially towards the wing tip where the aileron is located. Although this effect to some extent is compensated for by the winglets, the over-prediction of the magnitude is evident. An aerodynamic model based directly on Theodorsen's lift and pitching moment resulted in an almost identical frequency response, indicating that the pressure distribution over the wing part of the wing–aileron section is the dominant contribution to the aerodynamic loads due to aileron motion.

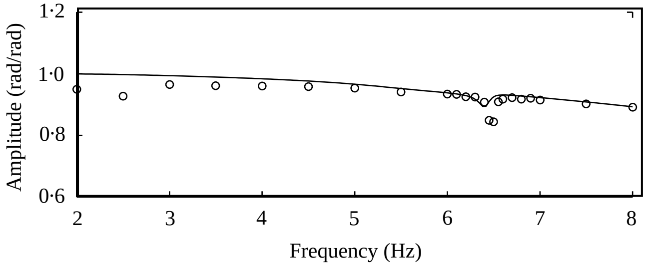

Figure 7. Amplitude of the aileron deflection at $\eta = \frac{3}{4}$: ○, measured; ——, predicted.

A control law design based on the present model would most likely fail due to the too optimistic influence of the aileron. The decision was thus made to introduce a model correction based on the open-loop results. The most obvious correction is to scale the right-hand side of the equations of motion (23) by a real factor to reduce the magnitude response without affecting the phase. The dashed magnitude response shown in Figure 6 is the result of scaling by a factor of 2, giving an updated model with satisfactory accuracy in the phase as well as magnitude. The described model correction was implemented in the closed-loop stability analysis by using the input vector

$$\mathbf{q}_m^* = \mathbf{q}_m/2 \tag{42}$$

instead of $\mathbf{q}_m$ in the closed-loop eigenvalue problem (37).

The coupling between the torsional deformation and the aileron deflection can be observed in the open-loop results. Figure 7 shows the amplitude of the measured aileron deflection (normalized with the setpoint amplitude) versus frequency. The torsional deformation of the wing at the resonance frequency results in a distinct dip in the measured aileron deflection. The solid curve represents the predicted amplitude of the aileron deflection at $\eta = \frac{3}{4}$, including the servo dynamics and hold delay. The descent of the amplitude due to the servo response is evident (compare with Figure 6), as well as the dip due to the coupling. Note that the coupling is proportional to $(1 - \eta)$, which means that the observed coupling is only $\frac{1}{4}$ the coupling at $\eta = 0$. The reason for the somewhat worse agreement between theory and experiment at low frequencies (where first mode bending is dominant) is most likely the neglected bending coupling.

4.3. CONTROL LAW DESIGN

Regardless of the control law used for suppressing the mode A flutter, the essential effect is that the eigenvalue $\hat{p}_A$ is shifted to the left in the root-locus plot in Figure 4. A straightforward approach to achieve this with the output feedback controller (36) is to minimize the real part of the eigenvalue $\hat{p}_A$ using the feedback gains in $\mathbf{k}$ as design variables. The maximum feasible level of actuation is enforced by constraining the squared norm of the feedback gain. For a fixed flow speed u the nonlinear optimization problem is posed as

$$\underset{\mathbf{k}}{\text{minimize}} \quad \mathscr{R}e\, \hat{p}_A(\mathbf{k}, u) \tag{43}$$

$$\text{subject to} \quad \mathbf{k}^{\mathrm{T}}\mathbf{k} \leq k_0^2, \tag{44}$$

where $\hat{p}_A$ is the eigenvalue obtained by solving the eigenvalue problem (37) with the correction (42), and the maximum feasible norm of $\mathbf{k}$ is denoted k_0. The optimization problem (43), (44) is solved using the method of moving asymptotes (MMA) by Svanberg (1993). The derivative of the objective function exists provided that the eigenvalues are distinct, and is derived as described in Haftka & Adelman (1993). Further, if a particular optimal solution $\mathbf{k}^*(u)$ exists on some interval of the flow speed u, the solution is continuous (but not necessarily continuously differentiable) on this interval, since both the eigenvalues and the quadratic constraint (44) are continuous functions of the feedback gains and flow speed, respectively (Ringertz 1997). Solving the optimization problem for a sequence of flow speeds u_i, $i = 1 \ldots n_u$, provides a set of optimal feedback gain vectors $\mathbf{k}_i^*(u_i)$ which are used for gain scheduling.

4.3.1. *Control system parameters*

By considering the servo response due to a given flutter motion of the wing, the norm k_0 can be related to the maximum aileron deflection δ_0 and rate $\dot{\delta}_0$ provided by the servo. Suppose that the wing oscillates with frequency Ω_0 at an amplitude with maximum output norm y_0. Taking the norm of the control law (36) and the first time derivative of it, the maximum feasible norm is obtained as

$$k_0 = \min\left\{\frac{\delta_0}{y_0}, \frac{\dot{\delta}_0}{\Omega_0 y_0}\right\}. \tag{45}$$

Effectively, this constraint means that the servo will not saturate for a flutter motion with frequency $\omega \leq \Omega_0$ and output norm $\|y\| \leq y_0$. If actuator saturation is not a concern, the constraint based on the maximum servo deflection (for a specified output norm) can be used to impose conditions for which the linear model is likely to be valid. Of course, if the flutter suppression is successful, the motion of the wing will remain small.

The measured displacements of markers 1–4 located on the wing (see Figure 3) were chosen for feedback. Based on $\delta_0 = 6°$ and $y_0 = 0{\cdot}01$ m, assumed to represent a motion in the linear regime, the maximum feasible norm $k_0 = 10\pi/3 \approx 10{\cdot}5$ rad/m was chosen. The maximum deflection and rate of the aileron were approximately 20° and 500°/s, respectively. Hence, for a flutter motion with frequency 6·4 Hz (the frequency of the mode A flutter) the servo will not saturate (in rate) until an output norm $y_0 \approx 0{\cdot}02$ m is reached.

To determine the sampling frequency T and computational delay Δ required in the modified aeroservoelastic model, a dummy control law based on linear interpolation for the gain scheduling was implemented in the experiment. In combination with the optical system, running in real-time mode, a 90 Hz closed-loop frequency was achieved. The sampling period $T = \frac{1}{90}$ s was thus used in the approximation of the sample-and-hold dynamics. An infrared sensor was used to measure the computational delay between a flash from the cameras and the arrival of the setpoint at the servo. The result was $\Delta = 24$ ms.

4.3.2 *Design optimization*

With the control system parameters settled, the optimization problem (43)–(44) was solved for the flow speeds $u = \{5, \; 5.2, \; 5.4, \ldots, 25\}$ m/s, giving a total of $n_u = 101$ problems to solve. The initial value $\mathbf{k} = \mathbf{0}$ was used for the first problem ($u = 5$ m/s), while for the successive problems the solution of the previous optimization was used as initial values. Each optimization run was terminated when the residual in the design variables was $< 10^{-4}$ (rad/m) between consecutive iterates. The first problem was solved in

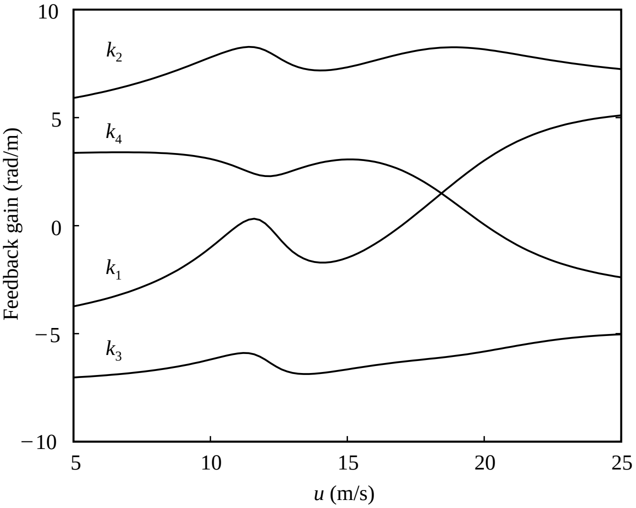

Figure 8. Optimal feedback gains versus flow speed.

approximately 20 iterations, while the remaining were solved in 5–10 iterations due to the more appropriate initial values.

The optimal feedback gains for the four marker displacements are plotted versus flow speed in Figure 8. The gain for marker 1 is denoted k_1 etc. The constraint (44) was active for all airspeeds, meaning that the controller uses full actuation throughout the considered speed range. Since markers 1 and 2 are located symmetrically with respect to the elastic axis, the deflection of the elastic axis at this spanwise location is proportional to the sum of the marker 1 and 2 displacements, while the twist angle is proportional to the difference. Considering the graphs for the corresponding gains in Figure 8, the result can be interpreted as if the control law emphasizes feedback of torsional deformation at low speeds and bending deformation at high speeds.

4.4. Closed-Loop Control

The closed-loop root-locus plot corresponding to the control law in Figure 8 is shown in Figure 9. Compared with Figure 4, the mode *A* root-locus is clearly shifted to the left. For the particular choice of feedback norm, the control law has only limited influence on the other modes. It should be emphasized that the influence on the other modes was not considered in the control law design. Unlike the open-loop case in Figure 4, mode *C* turns back in the speed range 11·4–13·2 m/s, but is then stabilized as before. The divergence mode *D* is actually stabilized by the control action. Mode *B*, which is hardly affected at all, is the mode that finally becomes unstable at the predicted critical speed $u_{\text{pred}} = 20{\cdot}8$ m/s. By coincidence, the wing is thus predicted to become unstable at the same critical speed as without control system, but this time in a 2·9 Hz bending–torsion flutter mode.

Experimentally, the controller performed well. The wing remained stable as the speed was increased above the open-loop flutter speed $u = 15{\cdot}4$ m/s. In Figure 10, the measured displacement of marker 2 (mid wing-trailing-edge) at $u = 18{\cdot}0$ m/s is shown for the cases with and without active control, respectively. With active control the displacement is visible as a small limit cycle motion, but the flutter is efficiently suppressed. This residual motion is expected due to both a finite resolution in the displacement measurements and a mechanical

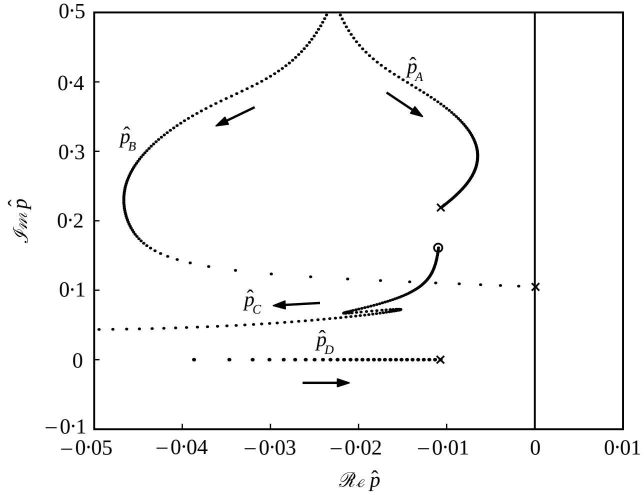

Figure 9. Closed-loop root-locus plot. The arrows indicate the direction of movement of poles with increasing flow speed u. The pole locations at the predicted critical speed are marked by "×".

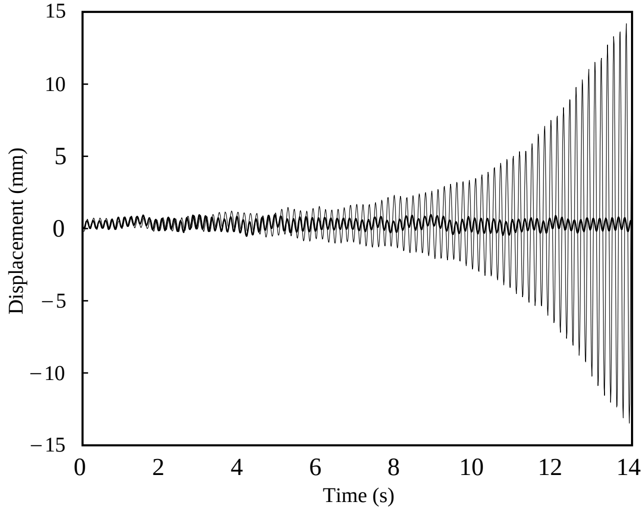

Figure 10. Displacement of marker 2 versus time at $u = 18$ m/s. With active control the displacement is visible as a small limit cycle motion. Without active control flutter develops within a few seconds.

play in the servo mechanism. The maximum amplitude of the residual motion was approximately 0·5 mm for all markers and considered speeds, which is of the same order as the subcritical response due to the flow disturbances in the wind tunnel. The result is therefore considered satisfactory. The scenario when the controller is turned off ($\delta = 0$) at $t = 0$ is shown by the superimposed graph in Figure 10. Violent flutter developed within a few seconds.

Although the linear theory used for the controller design lacks the capability of predicting the response after stability is lost, an experiment on the capability of the controller to suppress large-amplitude flutter was performed. Still at the speed $u = 18{\cdot}0$ m/s, the motion was allowed to grow by turning off the controller, after which the controller was turned on

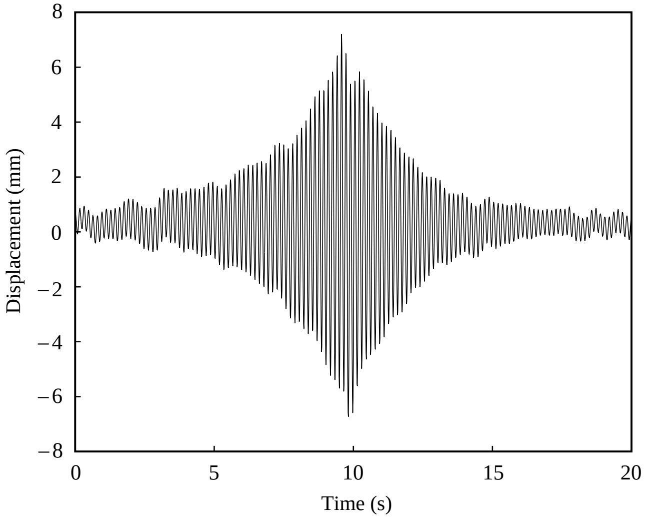

Figure 11. Experimental flutter suppression at $u = 18{\cdot}0$ m/s. The graph shows the displacement of marker 2 when the controller is turned off ($t = 0$) and on ($t \approx 10$).

again. The controller succeeded with this task as well, as shown by the marker 2 displacement in Figure 11.

Increasing the speed further, it was noted that the amplitude of the residual limit cycle motion shown in Figure 10 was reduced. This indicates that mode A is stabilized when the speed increases, as predicted in Figure 9. However, mode A flutter eventually developed if the controller was turned off. The wing finally suffered a 3·5 Hz bending–torsion flutter instability at the critical speed $u_{\text{exp}} = 23{\cdot}0$ m/s. Both the critical speed and the frequency of the aeroservoelastic flutter correspond well with the prediction.

4.5. Discussion of the Control Law Design

Since the prediction of the real part of the critical eigenvalue was somewhat inaccurate, closed-loop stability was not guaranteed prior to the experimental testing. For the particular choice of feedback norm the optimal control law did provide a shift of the critical eigenvalue sufficiently large to stabilize the mode A flutter in the experiment. However, increasing the maximum feasible feedback norm further results in a most significant influence on the modes not considered in the optimization.

To account for several modes in the optimization one may consider the minimax formulation

$$\underset{\mathbf{k}}{\text{minimize}} \max \mathscr{Re}\, \hat{p}_i(\mathbf{k}, u), \quad i = 1, \ldots, n_p \tag{46}$$

$$\text{subject to } \mathbf{k}^{\mathrm{T}}\mathbf{k} \leq k_0^2 \tag{47}$$

instead of equations (43) and (44). The minimax formulation (46) and (47) is inherently nonsmooth but is easily reformulated as a smooth optimization problem (Ringertz 1997). Unfortunately, a straight-forward application of the minimax formulation can result in a control law with very poor robustness to modelling uncertainties. Consider for example the present case where a mode is predicted to be stable but is actually unstable in the experiment. The optimizer may then focus on suppressing the wrong mode and the resulting controller will not stabilize the system in practice.

The use of optimization techniques for control law design is appealing, both in terms of being straightforward and that good performance can be obtained using quite simple control laws. In the present study only one parameter (the maximum feasible norm of the feedback gain) was set prior to the control law design. As indicated above, care must be taken when using optimization for design. To obtain a robust optimal control law, modelling deficiencies and system uncertainties have to be accounted for. This process first involves modelling and estimation of the uncertainties in the aeroservoelastic system (Lind & Brenner 1999) and then a reformulation of the optimization problem to take these into account. The formulation of optimization problems taking uncertainties into account is a current topic of research, discussed in for example Kuttenkeuler & Ringertz (1998*b*).

5. CONCLUSIONS

The rather simple aeroservoelastic analysis was found to predict the essential dynamics of the investigated system surprisingly well. Strip theory was verified by experimental open-loop testing to over-predict the response due to motion of the aileron. By introducing a straightforward model correction, based on the open-loop characteristics, sufficient accuracy for control law design was achieved.

The proposed control strategy was found to be successful. An approximately 50% increase of the critical speed was achieved in the experiment, which corresponds to more than a doubling of the critical dynamic pressure. However, it should be recognized that this significant improvement was made possible by the rather weak flutter instability. Suppressing the more aggressive mode *B* flutter would most likely require modifications of the control system and/or the wing itself (using for example multiple control surfaces).

It should be stressed that the external optical system used for capturing the structural deformation would not be possible to implement in a real flight situation. In general, dynamic output such as structural accelerations provided by properly located accelerometers would be better for controlling a flutter instability. However, evaluating the real-time capabilities of the optical system was an important part of this study. The system performed beyond expectation in terms of accuracy and robustness, and is undoubtedly a very useful tool in experimental aeroelasticity.

An interesting continuation of this work would be to investigate how a refined aeroelastic analysis based on plate theory and three-dimensional unsteady aerodynamics improves the results. A perhaps more interesting approach would be to develop an uncertainty model for the present system and perform a robust control law design. The present study indicates that the main source of uncertainty is the deficiencies of the model used for the unsteady aerodynamic loads, and also that effects due to structural damping and gravity can be neglected with maintained accuracy in the aeroservoelastic stability analysis. Further, it appears as if the pressure distribution over the wing part of the wing–aileron section is the dominant contribution to the aerodynamic loads due to aileron motion. Hence, using a model where the aerodynamic load on the aileron is transferred along the wing–aileron intersection is not only convenient but also a fairly good approximation of the true load transfer. The effect on the local aileron deflection due to wing–aileron elastic coupling was verified experimentally, and may be important to model if torsional deformation dominates the flutter modeshape.

ACKNOWLEDGEMENTS

Professor Ulf Ringertz is gratefully acknowledged for guidance and support. This work was financially supported by the Swedish Research Council for Engineering Sciences (TFR) and the National Program for Aeronautics Research (NFFP).

REFERENCES

BISPLINGHOFF, R. L., ASHLEY, H. & HALFMAN, R. L. 1996 Aeroelasticity. New York: Dover.

BORGLUND, D. 2000 Control and optimization of structures with fluid interaction. Ph.D. Dissertation, Report 2000-1, Department of Aeronautics, Kungliga Tekniska Högskolan, Stockholm, Sweden.

BÄCK, P. & RINGERTZ, U. T. 1997 On the convergence of methods for nonlinear eigenvalue problems. AIAA Journal **35,** 1084–1087.

COOK, R. D., MALKUS, D. S. & PLESHA, M. E. 1989 *Concepts and Applications of Finite Element Analysis.* New York: John Wiley & Sons.

EDWARDS, J. W., BREAKWELL, J. V. & BRYSON, A. E. 1978 Active flutter control using generalized unsteady aerodynamic theory. *Journal of Guidance and Control* **1,** 32–40.

GHIRINGHELLI, G. L., LANZ, M. & MANTEGAZZA, P. 1990 Active flutter suppression for a wing model. *Journal of Aircraft* **27,** 334–341.

HAFTKA, R. T. & ADELMAN, H. M. 1993 Sensitivity of discrete systems. In *Optimization of Large Structural Systems* (ed. G. I. N. Rozvany), Vol. **1**, pp. 289–311. Dordrecht: Kluwer. Academic Publishers.

HEEG, J. 1993 Analytical and experimental investigation of flutter suppression by piezoelectric actuation. NASA TP 93-3241, NASA.

JOHNSON, G. W. 1994 *LabVIEW Graphical Programming.* New York: McGraw-Hill.

KARPEL, M. 1982 Design for active flutter suppression and gust alleviation using state-space modeling. *Journal of Aircraft* **19,** 221–227.

KUTTENKEULER, J. 2000 Optical measurements of flutter mode shapes. *Journal of Aircraft* **37,** 846–849.

KUTTENKEULER, J. 1999 A finite element based modal method for determination of plate stiffnesses considering uncertainties. *Journal of Composite Materials* **33,** 695–711.

KUTTENKEULER, J. & RINGERTZ, U. T. 1998*a* Aeroelastic design optimization with experimental verification. *Journal of Aircraft* **35,** 505–507.

KUTTENKEULER, J. & RINGERTZ, U. T. 1998*b* Aeroelastic tailoring considering uncertainties in material properties. *Structural Optimization* **15,** 157–162.

LIND, R. & BRENNER, M. 1999 *Robust Aeroservoelastic Stability Analysis.* London Springer-Verlag.

LUTON, J. A. & MOOK, D. T. 1993 Numerical simulations of flutter and its suppression by active control. *AIAA Journal* **31,** 2312–2319.

MUKHOPADHYAY, V. (ed) 2000*a* Benchmark active control technology special section, Part I, *Journal of Guidance, Control and Dynamics* **23,** 913–960.

MUKHOPADHYAY, V. (ed) 2000*b* Benchmark active control technology special section, Part II, *Journal of Guidance, Control and Dynamics* **23,** 1093–1139.

MUKHOPADHYAY, V. (ed) 2001 Benchmark active control technology special section, Part III, *Journal of Guidance, Control and Dynamics* **24,** 146–192.

PAÏDOUSSIS, M. P. 1998 *Fluid–Structure Interactions—Slender Structures and Axial Flow.* London: Academic Press.

RINGERTZ, U. T. 1997 Eigenvalues in optimum structural design. In *Large-Scale Optimization with Applications* (eds Biegler, L. T., Coleman, T. F., Conn, A. R. & Santosa, F. N.), Vol. 92, pp. 135–149. New York. Springer-Verlag.

STEVENS, B. L. & LEWIS, F. L. 1992 *Aircraft Control and Simulation.* New York: John Wiley & Sons.

SVANBERG, K. 1993 The method of moving asymptotes (MMA) with some extensions. In *Optimization of Large Structural Systems* (ed. G. I. N. Rozvany), Vol. 1, pp. 555–566. Dordrecht Kluwer, Academic Publishers.

THEODORSEN, T. 1935 General theory of aerodynamic instability and the mechanism of flutter. NACA Report 496, NACA.

VIPPERMAN, J. S., CLARK, R. L., CONNER, M. & DOWELL, E. H. 1998 Experimental active control of a typical section using a trailing-edge flap. *Journal of Aircraft* **35,** 224–229.

WASZAK, M. R. & SRINATHKUMAR, S. 1995 Active flutter suppression for the active flexible wing. *Journal of Aircraft* **32,** 61–67.

WASZAK, M. R. & FUNG, J. 1996 Parameter estimation and analysis of actuators for the BACT wind-tunnel model. AIAA Paper 96-3362, *AIAA Atmospheric Flight Mechanics Conference*, San Diego, CA.

WEISSHAAR, T. A. & FOIST, B. L. 1985 Vibration tailoring of advanced composite lifting surfaces. *Journal of Aircraft* **22,** 141–147.

APPENDIX A: AERODYNAMIC INFLUENCE COEFFICIENTS

In the following, the unsteady aerodynamic forces acting on the aileron and wing partitions of a typical section are derived based on the work of Theodorsen (1935). Theodorsen considers a two-dimensional thin airfoil in an incompressible flow with freestream velocity u and density ρ. This is illustrated in Figure A1 with notation as defined in Section 2.1. Assuming simple harmonic motion with frequency ω, the unsteady pressure difference $\Delta p(x, t)$ between the pressures on the upper and lower sides of the airfoil is derived. In terms of the kinematic variables $q(t) = \{w, \theta, \delta\}$ the total lift $L(t)$ can be written as

$$L(t) = -\int_{-b}^{b} \Delta p \, \mathrm{d}x = \sum_{i=1}^{3} \rho(L_{\ddot{q}_i}\ddot{q}_i + uL_{\dot{q}_i}\dot{q}_i + u^2 L_{q_i}q_i). \tag{A1}$$

The total pitching moment $M(t)$ acting around the elastic axis (located at $x = ba$) and the aileron hinge moment $M^\delta(t)$ acting around the hinge axis (located at $x = bc$), are given by the corresponding sets of coefficients $\{M_{\ddot{q}_i} M_{\dot{q}_i} M_{q_i}\}$ and $\{M^\delta_{\ddot{q}_i} M^\delta_{\dot{q}_i} M^\delta_{q_i}\}$.

The separated formulation used in this work is obtained by partitioning the lift according to

$$L(t) = -\int_{-b}^{b} \Delta p \, \mathrm{d}x = -\int_{-b}^{bc} \Delta p \, \mathrm{d}x - \int_{bc}^{b} \Delta p \, \mathrm{d}x = L^w(t) + L^a(t), \tag{A2}$$

where $L^a(t)$ and $L^w(t)$ are the contributions from the aileron and wing, respectively. The pitching moment $M(t)$ can be separated in exactly the same manner, but the contribution $M^a(t)$ from the aileron is more conveniently written in the form

$$\begin{aligned} M^a(t) &= \int_{bc}^{b} (x - ba)\Delta p \, \mathrm{d}x = \int_{bc}^{b} (x - bc)\Delta p \, \mathrm{d}x \\ &\quad + \int_{bc}^{b} (bc - ba)\Delta p \, \mathrm{d}x = M^\delta(t) - b(c - a)L^a(t). \end{aligned} \tag{A3}$$

Since the aileron hinge moment $M^\delta(t)$ is known, only the lift $L^a(t)$ needs to be computed to obtain a separated two-dimensional formulation. The integrals involved in the computation of $L^a(t)$ are part of Theodorsen's derivation of the hinge moment, reducing the problem to a matter of extracting the coefficients $\{L^a_{\ddot{q}_i}, L^a_{\dot{q}_i}, L^a_{q_i}\}$. With these at hand, the coefficients for $L^w(t)$ and $M^w(t)$ follow from equation (A2) and the corresponding equation for the partitioning of the moment.

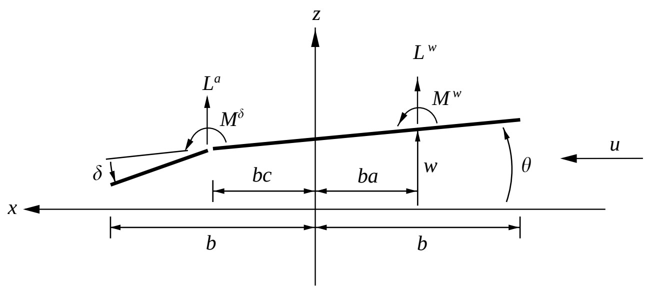

Figure A1. A thin airfoil in incompressible flow.

Based on Theodorsen's result the following constants are introduced:

$$
\begin{aligned}
&C_1 = \cos^{-1} c, && C_8 = 2cC_1C_2 - C_1^2 - C_2^2,\\
&C_2 = \sqrt{1-c^2}, && C_9 = \tfrac{1}{8}c(7+2c^2)C_2 - (\tfrac{1}{8}+c^2)C_1,\\
&C_3 = C_1 - C_2, && C_{10} = cC_1 - \tfrac{1}{3}(1+2c^2)C_2,\\
&C_4 = cC_1 - \tfrac{1}{3}(2+c^2)C_2, && C_{11} = \tfrac{1}{6}C_2^3 + \tfrac{1}{2}aC_7,\\
&C_5 = c(C_1^2 + C_2^2) - (1+c^2)C_1C_2, && C_{12} = C_1 + C_2,\\
&C_6 = \tfrac{1}{4}c(7+2c^2)C_1C_2 && C_{13} = (1-2c)C_1 + (2-c)C_2,\\
&\quad - (\tfrac{1}{8}+c^2)C_1^2 - \tfrac{1}{8}(5c^2+4)C_2^2, && C_{14} = (2+c)C_2 - (1+2c)C_1,\\
&C_7 = cC_2 - C_1, && C_{15} = -\tfrac{1}{2}C_9 - \tfrac{1}{2}(c-a)C_4.
\end{aligned}
\tag{A4}
$$

The coefficients for $L(t)$ and $L^a(t)$ may then be written as

$$
\begin{aligned}
&L_{\ddot w} = -\pi b^2, && L^a_{\ddot w} = b^2 C_7,\\
&L_{\dot w} = -2\pi b C(k), && L^a_{\dot w} = -2b\{C_3C(k) + C_2\},\\
&L_w = 0, && L^a_w = 0,\\
&L_{\ddot\theta} = -\pi b^3 a, && L^a_{\ddot\theta} = 2b^3 C_{11},\\
&L_{\dot\theta} = \pi b^2\{(1-2a)C(k)+1\}, && L^a_{\dot\theta} = -b^2[C_7 - (1-2a)\{C_3C(k)+C_2\}],\\
&L_\theta = 2\pi b C(k), && L^a_\theta = 2b\{C_3C(k)+C_2\},\\
&L_{\ddot\delta} = -b^3C_4, && L^a_{\ddot\delta} = -\tfrac{b^3}{\pi}C_5,\\
&L_{\dot\delta} = b^2\{C_{13}C(k) - C_7\}, && L^a_{\dot\delta} = -\tfrac{b^2}{\pi}[C_8 - C_{13}\{C_3C(k)+C_2\}],\\
&L_\delta = 2bC_{12}C(k), && L^a_\delta = -\tfrac{2b}{\pi}C_{12}\{C_3C(k)+C_2\};
\end{aligned}
\tag{A5}
$$

and likewise for $M(t)$ and $M^\delta(t)$:

$$
\begin{aligned}
&M_{\ddot w} = -\pi b^3 a, && M^\delta_{\ddot w} = -b^3C_4,\\
&M_{\dot w} = -\pi b^2(1+2a)C(k), && M^\delta_{\dot w} = b^2C_{14}C(k),\\
&M_w = 0, && M^\delta_w = 0,\\
&M_{\ddot\theta} = -\pi b^4(\tfrac{1}{8}+a^2), && M^\delta_{\ddot\theta} = -2b^4C_{15},\\
&M_{\dot\theta} = \pi b^3(\tfrac{1}{2}-a)\{(1+2a)C(k)-1\}, && M^\delta_{\dot\theta} = b^3[C_4 + 2C_{11}\\
&M_\theta = \pi b^2(1+2a)C(k), && \quad - (\tfrac{1}{2}-a)\{C_{14}C(k) - C_7\}],\\
&M_{\ddot\delta} = b^4\{C_9 + (c-a)C_4\}, && M^\delta_\theta = -b^2C_{14},\\
&M_{\dot\delta} = -b^3[C_4 - C_{10} - (c-a)C_7 && M^\delta_{\ddot\delta} = \tfrac{b^4}{\pi}C_6,\\
&\quad - C_{13}\{(\tfrac{1}{2}+a)C(k) - \tfrac{1}{2}\}], && M^\delta_{\dot\delta} = -\tfrac{b^3}{2\pi}C_{13}\{C_{14}C(k) - C_7\},\\
&M_\delta = -b^2[C_7 - C_{12}\{(1+2a)C(k)-1\}], && M^\delta_\delta = -\tfrac{b^2}{\pi}[C_8 + C_{12}\{C_{14}C(k) - C_7\}].
\end{aligned}
\tag{A6}
$$

The dependence on the reduced frequency of oscillation $k = \omega b/u$ is determined by Theodorsen's function $C(k)$, which can be written in terms of Hankel functions of the second kind, as

$$
C(k) = \frac{\mathrm{H}_1^{(2)}(k)}{\mathrm{H}_1^{(2)}(k) + \mathrm{i}\mathrm{H}_0^{(2)}(k)}.
\tag{A7}
$$